Semiconductor Scintillator for 3-Dimensional Array of Radiation Detectors

Serge Luryi and Arsen Subashiev
Dept. of Electrical and Computer Engineering, State University of New York, Stony Brook, NY 11794-2350, U.S.A.

1. Introduction

There are two large groups of solid-state radiation detectors, which dominate the area of ionizing radiation measurements, scintillation detectors and semiconductor diodes. The scintillators detect high-energy radiation through generation of light which is subsequently registered by a photo-detector that converts light into an electrical signal. Semiconductor diodes employ reverse biased p-n junctions where the absorbed radiation creates electrons and holes, which are separated by the junction field thereby producing a direct electrical response. Both groups are extensively reviewed in the classical treatise by Knoll.[1]

Most scintillators reported in the literature are implemented in wide-gap insulating materials doped ("activated") with radiation centers. A classical example of a solid-state scintillator is sodium iodide activated with thallium (NaI:Tl), introduced by Hofstadter[2] more than 60 years ago.

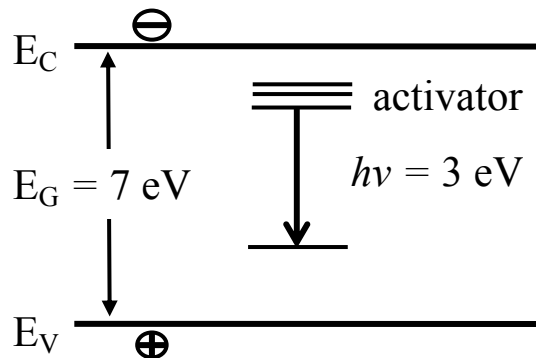The typical band diagram of a solid-state scintillator is shown in Fig. 1.

Figure 1. Conventional solid-state scintillator. Schematic energy band diagram of the thallium activated sodium iodide. Electrons and holes generated across the bandgap E_G migrate to the nearest activation site and recombine there emitting much lower photon energy $h\nu$.

Because of the much longer wavelength of the scintillation associated with the activator energy levels — compared to the interband absorption threshold — the insulating scintillators are very transparent to their own luminescence. However, this advantage comes at a price in the transport of carriers to the activator site. Individual carriers have very poor mobility in insulators and transport efficiency requires that the generated electrons and holes form excitons and travel to the radiation site as neutral entities. Therein lies a problem. The energy resolution even in the best modern scintillators does not compare well with that in semiconductors.[4] One of the fundamental reasons for poor resolution is that the luminescent yield in dielectric scintillators is controlled by reactions that are nonlinear in the density of generated electron-hole pairs, such as the formation of excitons at low densities and the Auger recombination at high densities.[5-8]

It is important to stress that such nonlinear processes do not exist in direct-gap doped semiconductors, where interaction with gamma radiation induces *minority* carriers while the concentration of majority carriers does not measurably change. Every reaction on the way to luminescence, including Auger recombination, is *linear* with respect to the concentration of minority carriers. One can therefore expect, as a matter of principle, that doped semiconductor scintillators will not exhibit effects of non-proportionality and their ultimate energy resolution could be on par with that of diode detectors implemented in the same material.

Normally, scintillators are not made of semiconductor material. The key issue in implementing a semiconductor scintillator is how to make the material transmit its own infrared luminescence, so that photons generated deep inside the semiconductor slab could reach its surface without tangible attenuation. However, semiconductors are usually opaque at wavelengths corresponding to their radiative emission spectrum. Our group has been working on the implementation of high-energy radiation detectors based on direct-gap semiconductor scintillator wafers, like InP or GaAs. For the exemplary case of InP the scintillation spectrum is a band of wavelengths near 920 nm. The original idea was to make InP relatively transparent to this radiation by doping it heavily with donor impurities, so as to introduce the Burstein shift between the emission and the absorption spectra.[9] Because of the heavy doping, the edge of absorption is blue-shifted relative to the emission edge by the carrier Fermi energy. Unfortunately, Burstein's shift by itself does not seem to provide adequate transparency at room temperature. The problem is that attenuation of the signal depends on depth of the interaction site into the semiconductor. The problem is discussed in Sect. 3 and its resolution in Sect. 4.

The transparency issue is of critical importance and we are concerned with new ways to further enhance the photon delivery to the semiconductor surface. One of the key new ideas is discussed in this paper. It is based on the extremely high radiative efficiency of high-quality direct-gap semiconductors. This means that an act of interband absorption does not finish off a scintillation photon; it merely creates a new minority carrier and then a new photon in a random direction. The efficiency of photon collection in direct-gap semiconductors is therefore limited only by parasitic processes, such as nonradiative recombination of the minority carriers and free-carrier absorption of light. The "ideal" semiconductor scintillator based on photon recycling is discussed in Sect. 5.

The proportionality of scintillation yield is not the only expected advantage of semiconductor scintillators. One of the major benefits of using semiconductor materials is the mature technology that enables the implementation of epitaxial photodiodes integrated on the surface of a semiconductor slab. An external receiver, like a photomultiplier, is not a viable option because of the complete internal reflection of most of the scintillating radiation. Owing to the high refractive index of semiconductors, e.g., $n = 3.3$ for InP, most of the scintillating photons will not escape from the semiconductor but suffer a complete internal reflection. Only those photons that are incident on the semiconductor-air interface within a narrow cone $\sin \theta < 1/n$ off the perpendicular to the interface, have a chance to escape from the semiconductor. The escape cone accommodates only a small fraction of isotropic scintillation, $\sin^2 \theta/2 < 1/4n^2 \approx 2\%$, whence the inefficiency of collection.

It is therefore imperative to integrate the scintillator wafer with a photodetector that has a substantially similar or even higher refractive index in an optically tight fashion. In collaboration with Sarnoff Corporation, our group has achieved substantial progress with *epitaxial photodetectors* on InP scintillator body, implemented as ultra-low leakage *pin* diodes based on quaternary InGaAsP materials.[10] These material layers of 1.24 eV bandgap are grown epitaxially on lattice-matched InP scintillator body and are sensitive to InP scintillation at the wavelength of 0.92 μm ($h\nu = 1.35$ eV). The epitaxial diode provides nearly perfect registration efficiency of photons that have reached the heterointerface. This in turn enables three-dimensional (3D) integration of scintillator "voxels" (3D pixels) that is illustrated in Fig. 2 and discussed in the next section (Sect. 2).
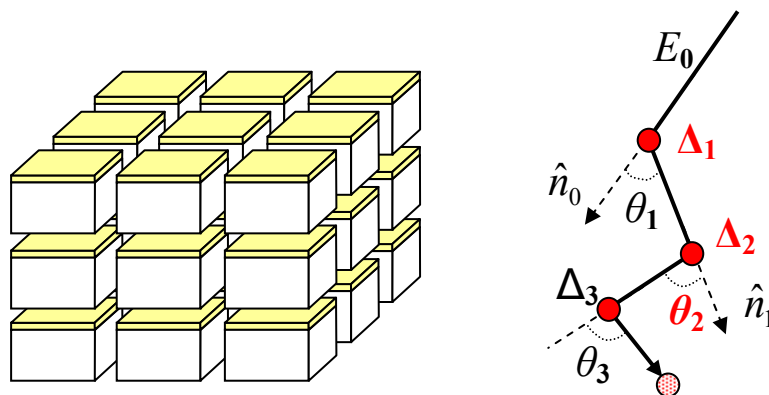

Figure 2. Schematic illustration of a 3D scintillator array. Each unit is a voxel comprising a scintillator body (shown as white slab) and an integrated photodiode (top plate) on its surface. Advantageously, the voxel may include two photodiodes integrated on *both* surfaces in an optically-tight fashion.

An incident gamma photon produces a cluster of firing pixels that report their positions and the energy deposited. The information reported enables one to determine both the incident photon energy and the direction to the source.

The diagram illustrates the track of a gamma photon of diminishing energy upon several successive Compton interactions producing a cluster of firing voxels.

2. Three-dimensional array of scintillator voxels: a Compton telescope

A stack of individually contacted 2D pixellated semiconductor slabs forms a 3D array of scintillator voxels, as illustrated in Fig. 2. This is the key concept of interest to us. A gamma photon incident on such an array undergoes several Compton interactions depositing varying amounts of energy Δ_i in voxels with coordinates $r_i = (x_i, y_i, z_i)$. The information reported enables one to determine both the incident photon energy and the direction to the source.

The exact relativistic kinematics of Compton scattering provides two equations at each interaction site illustrated in the diagram in Fig 2,

$$\Delta_i = E_{i-1} - E_i$$
$$\cos\theta_i = 1 + E_{i-1}^{-1} - E_i^{-1} \tag{1}$$

where all energies are expressed in units of electron rest energy, $m_e c^2 = 511$ keV. With three points r_i identified in the correct order (i=1,2,3) the set of equations (1) enables one to deduce both the incident energy and the incident direction cosine from the known energies Δ_1 and Δ_2 deposited in the first two pixels and the direction θ_2 to the third pixel, cf. the diagram in Fig. 2:

$$E_0 = \Delta_1 + \frac{\Delta_2}{2} + \frac{1}{2}\left(\Delta_2^2 + \frac{4\Delta_2}{1 - \cos\theta_2}\right)^{1/2} \tag{2a}$$

$$\cos\theta_1 = 1 + \frac{1}{E_0} - \frac{1}{E_0 - \Delta_1} \tag{2b}$$

Directionwise, the point source is placed on the cone of angle θ_1 about the measured direction n_1. Intersection of two or three such measurements gives the direction to the source. This technique is known as the Compton telescope.[11-13]

In contrast to gamma spectroscopy by conventional non-pixellated detectors,[1] a 3D array does not need to capture the entire incident gamma photon energy E_0 in order to determine E_0. However, the technique works only to the extent that one can order the events. Measurement of a fourth point in the cluster adds two equations and only one unknown and therefore can be used to determine the correct sequence. If all the measured quantities had a mathematical precision, the system of equations would be consistent only for the correct order. In practice, because both the positions and energies are measured only to within a certain margin of accuracy, the determination of the best order (referred to as the tracking algorithm or the event reconstruction) becomes a statistical procedure that minimizes inconsistency. Current tracking algorithms claim up to 70% success in correctly ordering events produced by a high-energy photon, by including in the analysis, besides the Compton kinematics, the anisotropic scattering cross-sections, expressed by the well-known[1] Klein-Nishina formula.

Semiconductor scintillators offer a tantalizing possibility of implementing a compact low-voltage Compton telescope.

3.   Problems with scintillator based on Burstein shift

The original idea of Burstein-shift based scintillator[9] is illustrated in Fig. 3.
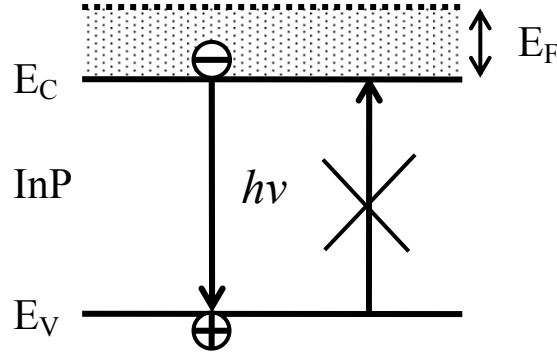

Figure 3. Schematic band diagram of a direct-gap semiconductor scintillator based on the Burstein shift (after Ref. 9). The semiconductor (InP) is doped n-type with degenerate doping concentration $N_D > 10^{18}$ cm^{-3}. The minority carriers (holes) are expected to recombine radiatively with electrons at the bottom of the Fermi sea. Absorption of thus emitted photons is largely suppressed.

Thermalized minority carriers (holes) are distributed near the top (within kT) of the valence band occupying a narrow range of wavenumbers, $\hbar q \sim (2 m_h kT)^{1/2}$. Conservation of momentum in radiative transitions requires that participating electrons have the same wavenumber and leads to an expected spectrum of emitted photons $hv \sim E_G + \Delta E$ of width $\Delta E \sim kT (m_{h/} m_e + 1)$. However, experimentally the emission spectrum $S(E)$ of heavily doped InP is wider (of width about $E_F > \Delta E$) and it does not substantially narrow at cryogenic temperatures. This suggests that in our heavily doped samples momentum is not conserved and the entire Fermi sea of electrons contributes to the spectrum, cf. Fig. 4.

The Burstein shift does provide an enhanced transparency but it has not proven sufficient for the intended application. In n-type InP with donor concentration of $N_D = 6 \times 10^{18}$ cm^{-3} at room temperature, the mean free path of photons averaged over the fundamental emission spectrum, is about 100 μm. That is obviously not enough. However, InP has a high radiative efficiency η (over 90%) and those photons that are absorbed generate another electron-hole pair that recombines producing a new photon. We shall discuss this photon recycling process in more detail in Sect. 3. At this point, however, it can be noted that once photon recycling is of the essence, one cannot expect that heavily-doped samples are necessarily best. The optimum doping concentration is controlled by (a) the free-carrier absorption of light that obviously favors low doping , (b) the radiative efficiency where verdict depends on the dominant mechanism of non-radiative recombination, and (c) the transparent fraction of the spectrum $S(E)$ that may benefit form the Burstein shift.
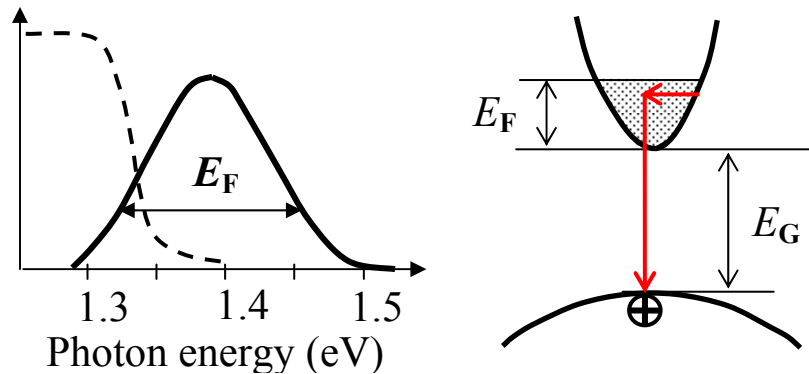
Figure 4. Schematic illustration of spectra *S(E)* observed in heavily doped InP (solid line). The dashed line indicates the transparency of the sample (on a logarithmic scale). The right-hand panel illustrates the radiative transitions that do not conserve quasi-momentum in heavily-doped material.

Photon recycling can deliver a reasonable fraction of the scintillating photons to the wafer surface. However, this fraction depends on the exact position of the interaction site relative the surface and this constitutes a major problem for the accurate determination of the deposited energy. The problem is how to distinguish the signal arising from a large energy deposited far from the photoreceiver surface from that arising from smaller energy deposited nearby.

The problem arises from the attenuation of the optical signal. If we knew the distance *z* of the gamma interaction event from the photoreceiver surface, one could correct for the attenuation. Recently, we came up with an idea how to do this.[14] The idea is based on two-sided photo detection by implementing epitaxial photo-diodes on both sides of the InP scintillator wafer. The simultaneous detection by *both* detectors of the scintillation arising from the same interaction event, allows us to determine the position of the interaction and therefore correct for attenuation.

4.   Double-sided detection

Consider a scintillator slab, Fig. 5, endowed with two arrays of photodetectors and two read-out circuits on the opposite sides of the slab. An essential ingredient of the proposed approach is the ability to extract the event position, characterized by a distance *z* from one of the slab surface, by analyzing the two photoreceiver signals from the same ionization event. It has been ascertained by our calculations that it is sufficient to know the ratio of the two signals to make an accurate estimate of the event position. Another essential ingredient is the ability to correct for the attenuation after the position has been ascertained. Both of these capabilities can be obtained by calculations coupled with experimental validation.

In heavily doped InP the attenuation is due to *losses* – of photons in free-carrier absorption and minority carriers in non-radiative recombination. However, the ratio of attenuated signals is not sensitive to these losses, see Sect. 5.
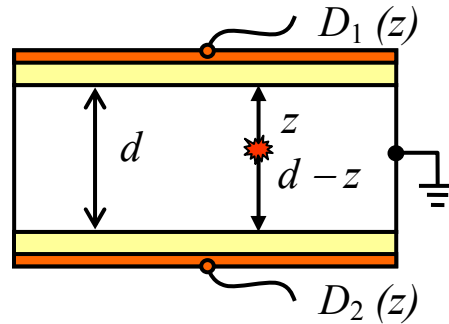
Figure 5. Schematic cross-section of an InP scintillator with two epitaxial InGaAsP photodiodes grown on both sides. Exemplarily, d = 350 μm, while the thickness of epitaxial diodes is $\approx$ 2 μm (exaggerated in the figure). Lateral dimensions of the scintillator are about 1 mm.

Suppose an interaction event (shown by the explosion symbol in Fig. 5) occurs at a distance z from the top surface. As a result, both the top and the bottom photo-detectors will produce a signal. The calculated ratio $\rho(z) = D_2/D_1$ of these two signals is plotted in Fig. 6 for different doping levels. It is assumed that the photodiodes themselves are ideal and identical on both sides. Figure 6 shows that simultaneous measurement of the responses D_1 and D_2 gives sufficient information to locate the position z of the interaction event.
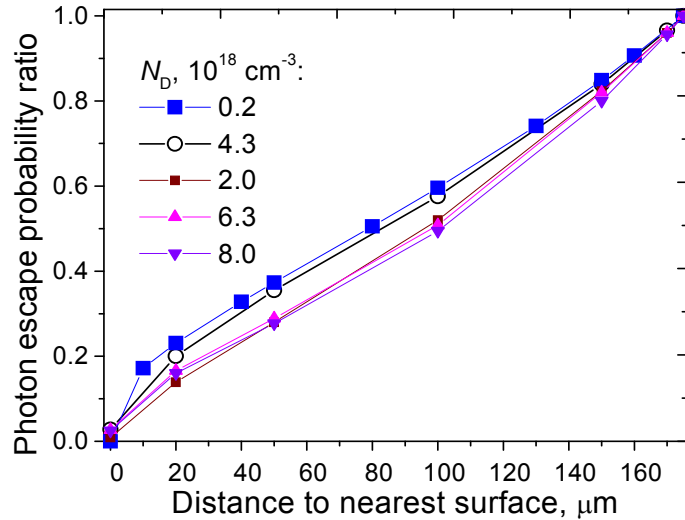

Figure 6. Calculated (see Eq. 9 below) ratio of the two signals recorded by two surface detectors for the same radiation event for different doping levels in the scintillator body. The scintillator thickness is d = 350 μm as in Fig. 5, and the ratio is shown for $z \leq d/2$, since by symmetry, one has $\rho(z) = \rho^{-1}(d-z)$.

5. Scintillator based on photon recycling

In high-quality direct-gap semiconductors most of the scintillation photons reaching the detectors surface are not photons directly generated by the electrons and holes at the site of the gamma particle interaction, but photons that have been re-absorbed and re-emitted a multiple number of times. This phenomenon, called the photon recycling, was introduced by Dumke[15] and Moss[16] and used by Asbeck[17] to explain the long radiative lifetime in GaAs/AlGaAs heterostructure is often discussed in connection with high-efficiency light emitting diodes.[18] It is essential for understanding the properties of our direct-gap semiconductor scintillator.

Traditionally, an ideal scintillator requires material that is highly transparent to its own luminescence. For example, one can imagine doping the semiconductor with high efficiency radiative centers that emit below-bandgap light. It is important that the excited electron-hole pairs are efficiently transferred to the radiative center. In the case of InP, this energy transfer probability was shown[19] to be high for certain trivalent luminescent ions incorporated in the host lattice. The system InP:Yb^{3+} seems to work well at cryogenic temperatures, producing emission near 1 μm – well below the bandgap of InP. However, at room temperature, its performance is degraded by fast non-radiative de-excitation of Yb ions.[19] Other ideas for implementing *transparent* semiconductor scintillators include replacing luminescent ions by semiconductor "impregnations" of lower bandgap.[20]

In the presence of multiple photon recycling one can have another kind of ideal (*nontransparent* but lossless) scintillator, as we shall now discuss.

Let the luminescent signal comprise the energy spectrum $S(E) = GS_0(E)$ (where S_0 is normalized to unity, $\int S_0(E)\,dE = 1$). The signal is assumed to be generated a distance z from the detector top surface, as indicated in Fig. 5. The emitted energy is isotropic, so that the energy emitted in unit energy interval per unit solid angle is $(G/4\pi)\,S_0(E)$. The total energy $D_i(z)$ reaching the i-th detector surface ($i=1, 2$) is attenuated in a way that depends on z.

In the presence of absorption, characterized by the interband absorption coefficient $\alpha_i(E)$, the detection probability for a photon at energy E (averaged over all angles) is given by

$$\pi(E,z) = \int_0^\infty \exp[-\alpha_i(E)r]\frac{\cos\theta}{2r^2}\,\rho\,d\rho, \qquad (3)$$

where $\rho = z\tan\theta$ and $r = z/\cos\theta$. Averaged over the emitted photon spectrum $S(E)$, the probability p_1 that the photon reaches detector 1 at $z = 0$ is given by

$$p_1(z) = \int \pi(E,z)\,S(E)\,dE. \qquad (4)$$

We shall refer to the probability (4) and the similar probability $p_2(z) = p_1(d-z)$ that the photon generated at point z reaches detector 2 at $z = d$, as *single-pass* probabilities, because they do not include the subsequent fate (recycling) of the absorbed photon. The probability (4), calculated using experimental spectra $S(E)$ for different doping levels in InP, is shown in Fig. 7.
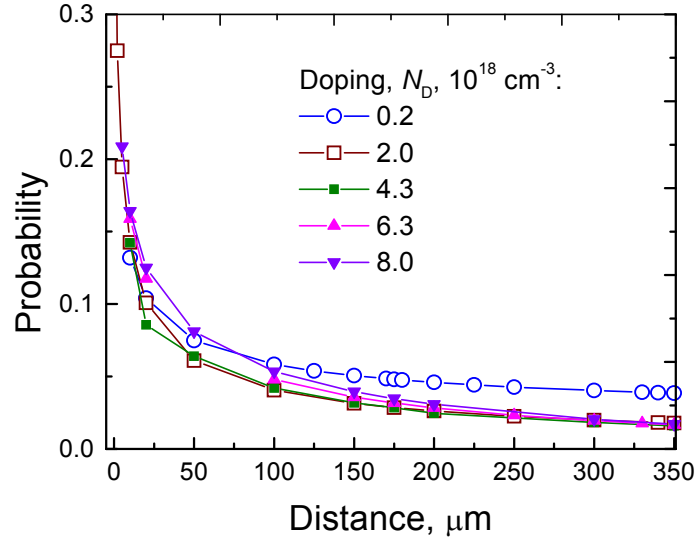
Figure 7. Single-pass photon escape probability p_1 (z) calculated for an exemplary 350 μm InP layer, doped n-type at different doping levels. The probabilities are plotted as functions of the distance from the interaction site to the integrated photodiode surface. The calculation is based on measurements of the absorption spectra in these crystals.

The single-pass probability p_{fca} of free-carrier absorption (FCA) describes the importance of these parasitic lossy processes relative to interband absorption. It can be estimated by neglecting both p_1 and p_2, while keeping the dominant process of interband absorption, viz.

$$p_{fca} \approx \int \frac{\alpha_e}{\alpha_e + \alpha_i} S(E)\, dE \,, \qquad (5)$$

where α_e (E) is the FCA absorption coefficient, primarily owing to intervalley electronic transitions.[19] Both α_i and α_e depend on the doping level, the former through the Burstein shift and the latter is directly proportional to the number of majority carriers.

Consider the basic processes in an InP scintillator with two photodiode surfaces, as in Fig. 5. The minority carrier ("hole" h) initially created by the ionizing interaction has the probability η (radiative efficiency) to generate a photon (of energy spectrum S). The generated photon can either reach detectors 1 and 2 (designated by probabilities p_1 and p_2, respectively) or disappear through FCA (probability p_{fca}). All these probabilities depend on the position z (the spectral dependence can be eliminated by averaging over S). The combined probability $P(z)=p_1+p_2+p_{fca}$ describes the likelihood of the photon loss at this stage, and the alternative, $1-P(z)$, is the probability that a new hole is created through interband absorption. The cycle of hole-photon-hole transformation repeats *ad infinitum,* as illustrated in the diagram in Fig. 8.
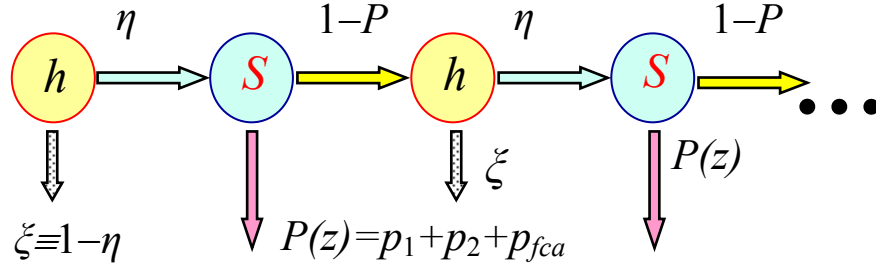
Figure 8. Schematic diagram of the basic processes in an InP scintillator with two photodiode surfaces.

So long as the photon recycling process continues, the minority carriers (holes) and photons are interchangeable entities. The process can be finished off by FCA (with the probability p_{fca}) while the entity is photon or, while the entity is hole, by nonradiative transitions that occur with the small probability $\xi = 1 - \eta$ (in our samples η ranges from 90% to 99%). Needless to say, the process can also have a happy end (photon detected). The radiative efficiency is defined in terms of the rates of radiative (ν_r) and nonradiative (ν_{nr}) transitions, viz.

$$\eta = \frac{\nu_r}{\nu_r + \nu_{nr}}. \qquad (6)$$

The total signal in detector 1 is a sum of the single-pass contributions from different cycles of photon regeneration. As is evident from Fig. 8, it can be summed as a geometric progression, giving

$$D_1(z) = G\eta\, p_1(z) \times \sum_{n=0} [\eta(1-P)]^n = \frac{G\eta\, p_1(z)}{\xi + \eta\, P(z)}. \qquad (7)$$

Similarly, the total signal in detector 2 is given by

$$D_2(z) = G\eta\, p_2(z) \times \sum_{n=0} [\eta(1-P)]^n = \frac{G\eta\, p_2(z)}{\xi + \eta\, P(z)}. \qquad (8)$$

Equations (7) and (8) express the attenuated signal in terms of single pass probabilities and the photon recycling parameters η and p_{fca}. However, the *ratio* of the two signals depends only on the single-pass probabilities,

$$\rho(z) \equiv \frac{D_2(z)}{D_1(z)} = \frac{p_2(z)}{p_1(z)}, \qquad (9)$$

which are controlled by the spectral dependence of the *interband* absorption only, as is evident from Eqs. (3) and (4). The calculated signal ratio (9) with p_1 and p_2 as in Fig. 7, was plotted in Fig. 6 above.

It is important to note that for high photon recycling ($\eta \to 1$ and $p_{fca} \to 0$) one has an ideal scintillator in the sense that all generated photons are collected – even though the single-pass probabilities p_1 and p_2 may not be high due to interband absorption. However, the interband absorption does not "kill off" the photon because another minority carrier is created. In a sample with high η another photon will re-emerge to make a new try at reaching one of the detectors. If the FCA is also low, *all photons will be eventually collected* in this way.

Let us emphasize that in such an ideal scintillator the ratio of signals will still depend on the position z of the interaction, cf. Eq. (9). This extends the validity of the two-sided detection concept to the case of a perfect scintillator based on photon recycling. In the case of such a perfect scintillator, the value of two-sided detection is not only that it provides a factor of 2 to the overall number of photons collected, but it also provides the position identification *not limited* to the vertical dimension of the pixel. One can have a thick pixel and still resolve the vertical position from the pre-calibrated ratio (9).

An important parameter for scintillator applications in gamma-spectroscopy is the photon collection efficiency (PCE),

$$\text{PCE} \equiv \frac{D_1(z) + D_2(z)}{G}. \tag{10}$$

The PCE is generally less than unity, due to the above discussed loss processes. From Eqs. (7) and (8) we find that the total PCE is given by

$$\text{PCE} = \frac{p_1(z) + p_2(z)}{\left[(v_{nr}/v_r) + p_{fca}(z) \right] + \left[p_1(z) + p_2(z) \right]}. \tag{11}$$

6. How close are we to an ideal semiconductor scintillator?

As is clear from Eq. (11), implementation of an ideal scintillator based on photon recycling requires (*a*) high radiative efficiency ($\eta \to 1$ or. $v_{nr}/v_r \ll 1$), (*b*) low free-carrier absorption ($p_{fca} \to 0$), and (*c*) reasonable transparency, expressed by nonvanishing single-pass probabilities, $p_1(z)_+ p_2(z) \geq 2 p_1(d/2)$.

Optimization of the condition (*a*) depends on the nature of non-radiative recombination. The total minority-carrier recombination rate is given by

$$v_{tot} = A + Bn + Cn^2, \tag{12}$$

where n is the majority-carrier concentration provided by the doping ($n = N_D$ at room temperature). Term A describes a non-radiative mechanism due to unintended acceptor-like impurities, whose concentration N_A (and hence v_{nr}) is independent of N_D, term B describes the radiative rate v_r, and term C describes the Auger nonradiative recombination mechanism.

If the dominant non-radiative mechanism is A, then one would expect the optimum to be at higher N_D, since the radiative rate $v_r \sim N_D$. If, on the other hand, the dominant nonradiative mechanism is due to Auger recombination ($v_{nr} \sim N_D^2$), then one should seek the optimum at lower concentrations.

Our experimental results clearly favor the Auger mechanism, see. Fig. 9. The solid line is a fit to the recombination rates given by Eq. (12), with the radiative (B) and Auger (C) coefficients taken from our luminescence experiments (these are close to the room-temperature date reported in the literature,[22] within their margin of accuracy) and a fitted coefficient A. The low-doped samples have evidently higher radiative efficiency, with a maximum of about 99% at $N_D \approx 2 \times 10^{17}$ cm^{-3}. At still lower concentrations, one can expect η to drop due to term A.
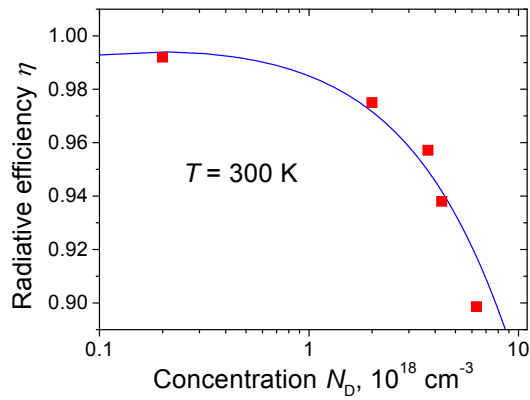

Figure 9. Room-temperature radiative efficiency as function of majority-carrier concentration provided by the doping. The solid line describes a fit to Eq. (12) with $A = 2 \times 10^5$ s^{-1}, $B = 1.9 \times 10^{-10}$ cm^3 s^{-1}, and $C = 1.5 \times 10^{-30}$ cm^6 s^{-1}.
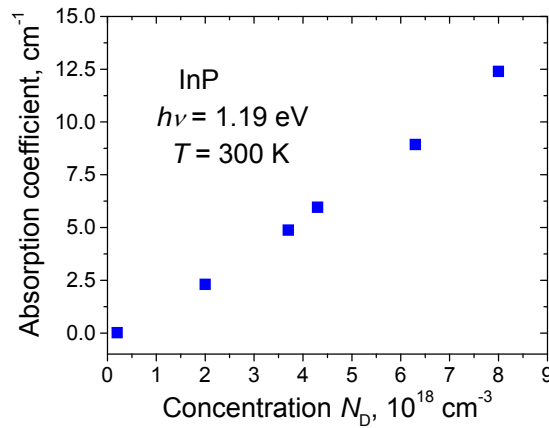

Figure 10. Free-carrier absorption coefficient, α_e, measured in our InP samples. At the lowest concentration $N_D \approx 2 \times 10^{17}$ cm^{-3}, one has $\alpha_e < 0.1$ cm^{-1}.

Condition (*b*) is clearly favored by *lower* doping concentrations, cf. Fig. 10. For $N_D \approx 2\times10^{17}$ cm^{-3}, the FCA absorption is very small, $\alpha_e < 0.1$ cm^{-1}, and the probability p_{fca} can be neglected.

Finally, condition (c) – which had been the key consideration at the start of our work – depends primarily on the positioning of the interband absorption spectrum α_i (*E*) relative to the basic luminescence emission spectrum *S* (*E*), as evident from Fig. 4 and Eqs. (3) and (4). This is precisely the condition that we had sought to optimize with the Burstein shift. However, our theoretical considerations had led us to consider much lower concentration ranges, where the Burstein shift is inoperative. The experimentally observed luminescence spectra show that the low-doped (non-degenerate) sample with $N_D = 2\times10^{17}$ cm^{-3} is about ten times brighter than our best degenerately doped samples. In the low-doped sample both the quantum efficiency becomes high (due to the absence of Auger recombination) and the residual (free-carrier) absorption becomes very low. The feared drawback of low-doped samples, the tight overlap of the absorption and emission bands, is more than compensated by high photon recycling.

Once the conditions (*a-c*) are satisfied, the photon collection efficiency predicted by Eq. (11) is very high indeed, even when single-pass probabilities are low. With negligible free-carrier absorption $(p_{fca} \to 0)$ and the high radiative efficiency ($v_{nr}/v_r = 0.01$) featured by our low-doped InP samples, the PCE = 0.95 assuming the values p_1 (*z*) + p_2 (*z*) ≈ 0.2 estimated from our earlier experimental data. Even for still lower single-pass probabilities, viz. $2\,p_1$ (*d*/2) ≈ 0.1, estimated theoretically (see Fig. 7), one has PCE = 0.91. It should be noted that the theoretical estimate presented here gives a lower estimate for the PCE. More refined theoretical analysis, now in progress, will allow for (*i*) finite size of the initial excitation region, and (*ii*) expansion of the excitation region in the process of recycling. Both effects are expected to increase the PCE estimate. Inclusion of (*i*) is reasonably straightforward, provided one knows the spatial distribution *H* (*r*) of holes generated by the gamma photon. One would then simply average Eqs. (7) and (8) over *H* (*r*). Evaluation of *H* (*r*) is not a simple matter, however.[23,24]

Inclusion of the effect (*ii*) is more subtle, especially for the lower-doped samples. Our derivation of Eqs. (7) and (8) assumes that every act of recycling occurs at the same place *z* where the initial interaction occurred, and therefore the same probabilities p_1 (*z*) and p_2 (*z*) appear at all stages of the recycling, cf. Fig. 8. This has reduced the summation of an infinite series to a geometric progression and allowed us to obtain the result in a closed form. In reality, however, there is a transport of holes in photon recycling, which has the nature of a random walk. Recombination of a hole at a position *r* is accompanied by emergence of another hole at a *r* + $\boldsymbol{\ell}$, where $\boldsymbol{\ell}$ is a random vector, characterizing the free flight of an emitted photon. In a heavily doped sample this random walk reduces to diffusion with a diffusion coefficient $\sim \ell^2/\tau$, where τ is the radiative recombination time. For a sample with $N_D = 6\times10^{18}$ cm^{-3} we had estimated the mean-square unit flight ℓ to be of order 100 μm. For lightly-doped samples, however, the diffusion approximation breaks down because of the extreme transparency in the long wavelength wing of the spectrum *S* (*E*), where ℓ is limited by FCA only. For the

sample with $N_{\mathrm{D}} \approx 2 \times 10^{17}$ cm^{-3}, where $\alpha_e < 0.1$ cm^{-1}, one has $\alpha_e\, d << 1$, and nothing should change if we set $\alpha_e = 0$, which corresponds to diverging $\ell \to \infty$. Random walks, where the distribution of unit flights is so long-tailed that their second moment diverges, are known as Lévy flights.[25] An interesting example of optical Lévy flights was recently discussed by Barthelemy et al.[26] Such random walks with divergent average step length lead to the so-called *super-diffusion*, where the average squared displacement increases faster than linearly with time. As subtle as this may be, the super-diffusive behavior is likely to be of importance for estimating the photon collection efficiency. By a crude analogy with averaging over $H(r)$, we expect that the single-pass probabilities in Eq. (11) will be replaced by larger "effective" values

$$\widetilde{p}_i(z) > p_i(z) \, ,$$

that would enhance the PCE estimate. The enhancement is hard to estimate at this time and it requires further studies. The ultimate aim of these studies is an accurate estimate of the optimum scintillator layer thickness for best energy resolution.

7. Conclusions

As discussed in the introduction, the semiconductor scintillator does not suffer from the non-proportionality effects and its energy resolution is fundamentally limited by energy branching in the same way as it is for semiconductor diodes. However, high photon collection efficiency is an obvious prerequisite for the good energy resolution. We have shown that a semiconductor scintillator based on photon recycling is capable of delivering very high PCE, even though the material is not transparent in the usual sense to its own luminescence. In order to take advantage of photon recycling, double-sided integrated photodiodes appear necessary. We can ultimately expect the energy resolution of semiconductor scintillators to approach that of a diode detector implemented in the same material.

References

1. G. F. Knoll, *Radiation Detection and Measurement*, 3rd ed., Wiley, New York (2000).
2. R. Hofstadter, "Alkali Halide Scintillation Counters", *Phys. Rev.* **74**, pp. 100-101 (1948).
3. C. L. Melcher, "Perspectives on the future development of new scintillators," *Nucl. Instruments and Methods in Phys. Res.* **A 537**, pp. 6-14 (2005).
4. P. Dorenbos, "Light output and energy resolution of Ce^{3+}-doped scintillators," *Nucl. Instruments and Methods in Phys. Res.* **A 486**, pp. 208-213 (2002).
5. A. N. Vasil'ev, "From luminescence non-linearity to scintillation non-proportionality," *IEEE Trans. Nucl. Sci.* **55**, pp. 1054-1061 (2008).
6. G. Bizarri, W. W. Moses, J. Singh, A. N. Vasil'ev, and R. T. Williams, "An analytical model of nonproportional scintillator light yield in terms of recombination rates," *J. Appl. Phys.* **105**, 044507, pp. 1-15 (2009).
7. G. Bizarri, W.W. Moses, J. Singh, A.N. Vasil'ev, and R.T. Williams, "The role of different linear and non-linear channels of relaxation in scintillator non-proportionality," *Journal of Luminescence,* in press (2009).
8. S. A. Payne, N. J. Cherepy, G. Hull, J. D. Valentine, W. W. Moses, and W.-S. Choong, "Nonproportionality of scintillator detectors: theory and experiment," *IEEE Trans. Nucl. Sci.* **56**, pp. 2506-2512 (2009).
9. A. Kastalsky, S. Luryi, and B. Spivak, "Semiconductor high-energy radiation scintillation detector", *Nucl. Instruments and Methods in Phys. Res.* **A 565**, pp. 650-656 (2006).
10. S. Luryi, A. Kastalsky, M. Gouzman, N. Lifshitz, O. Semyonov, M. Stanacevic, A. Subashiev, V. Kuzminsky, W. Cheng, V. Smagin, Z. Chen, J. H. Abeles, W. K. Chan, and Z. A. Shellenbarger, "Epitaxial InGaAsP/InP photodiode for registration of InP scintillation", to be published.
11. E. Aprile, A. Bolotnikov, D. Chen, and R. Mukherjee, "A Monte Carlo analysis of the liquid xenon TPC as gamma-ray telescope", *Nucl. Instruments and Methods in Phys. Res.* **A 327**, pp. 216-221 (1993).
12. J.D. Kurfess, W.N. Johnson, R.A. Kroeger, and B.F. Phlips, "Considerations for the next Compton Telescope Mission", *Proceedings of the 5th Compton Symp.*, Portsmouth, NH (1999).
13. S.E. Boggs and P. Jean, "Event reconstruction in high resolution Compton telescopes", *Astron. Astrophys. Suppl. Ser.* **145**, pp. 311-321 (2000).
14. J. H. Abeles and S. Luryi, "Slab scintillator with integrated two-sided photoreceiver", US Pat. Provisional application, Ser. No. 61/216,572 (2009).
15. W. P. Dumke, "Spontaneous radiative recombination in semiconductors," *Phys. Rev.* **105**, pp. 139-144 (1957).
16. T. S. Moss, "Theory of the spectral distribution of recombination radiation from InSb," *Proc. Phys. Soc.* **B 70**, pp. 247-250 (1957).
17. P. Asbeck, "Self-absorption effects on the radiative lifetime in GaAs/AlGaAs heterostructures," *J. Appl. Phys.* **48**, pp. 820-822 (1977).

18. See, e.g., R. Windisch, C. Rooman, B. Dutta, A. Knobloch, G. Borghs, G. H. Döhler, and P. Heremans, "Light-extraction mechanisms in high-efficiency surface-textured light-emitting diodes," *IEEE J. Selected Topics in Quantum Electronics* **8**, pp. 248-255 (2002).

19. A. Taguchi and K. Takahei, "Trap level characteristics of rare-earth luminescence centers in III–V semiconductors", *J. Appl. Phys.* **79**, pp. 4330-4334 (1996).

20. S. Luryi, "Impregnated Semiconductor Scintillator", *International Journal of High Speed Electronics and Systems*, vol. **18**, No 4 pp. 973-982 (2008).

21. W. P. Dumke, M. R. Lorenz, G. D. Pettit, "Intra- and Interband Free-carrier Absorption and the Fundamental Absorption Edge in *n*-Type InP", *Phys. Rev.* **B1**, pp. 4668-4673 (1970).

22. See, e.g., Electronic Archive*: New Semiconductor Materials, Characteristics and Properties,* http://www.ioffe.rssi.ru/SVA/NSM/, maintained by the Ioffe Physico-Technical Institute.

23. E. Gros d'Aillon, J. Tabary, A. Glière, and L. Verger "Charge sharing on monolithic CdZnTe gamma-ray detectors: A simulation study," *Nucl. Instruments and Methods in Phys. Res.* **A 563**, pp. 124-127 (2006).

24. J. Hayward and D. Wehe, "Incomplete charge collection in an HPGe double-sided strip detector," *Nucl. Instruments and Methods in Phys. Res.* **A 586**, pp. 215-223 (2008).

25. See, e.g., R. Metzler, A. V. Chechkin V. Yu. Gonchar, and J. Klafter, "Some fundamental aspects of Lévy flights," *Chaos, Solitons & Fractals* **34**, pp. 129–142 (2007).

26. P. Barthelemy, J. Bertolotti, and D. S. Wiersma, "A Lévy flight for light," *Nature* **453**, pp. 495-498 (2008).